Applied Surface Science 719 (2026) 164983

Contents lists available at ScienceDirect

Applied Surface Science

journal homepage: www.elsevier.com/locate/apsusc

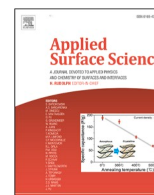

Full Length Article

A dry-wet quasi-ALE approach for transition metals: tungsten as a model system

Cinzia Chan [a,b,*], Jean-François de Marneffe [b], Christopher Gort [c], Jill Serron [b], Marta Agati [b], Felix Seidel [b], Jan P. Hofmann [c], Stefan De Gendt [a,b], Dennis H. van Dorp [b]

[a] *Department of Chemistry, Katholieke Universiteit Leuven, Celestijnenlaan 200F, Leuven 3000, Belgium*
[b] *Imec, Kapeldreef 75, 3001 Heverlee, Belgium*
[c] *Surface Science Laboratory, Department of Materials and Geosciences, Technical University of Darmstadt, Peter-Grünberg-Straße 4, 64287 Darmstadt, Germany*

ARTICLE INFO

Keywords:
Atomic layer etching
Transition metals
Selectivity
post operando XPS
ICP-MS

ABSTRACT

A dry-wet Quasi-ALE (Q-ALE) process is demonstrated for tungsten, combining self-limiting O_2 plasma oxidation with timed wet-chemical oxide removal in 1 M HCl solution at room temperature (RT). Inductively coupled plasma mass spectroscopy (ICP-MS) and electrochemical measurements were used to study oxide dissolution kinetics. Quantification revealed an initially high etch rate of the surface that gradually decreased and stabilized to a low background value. This evolution is attributed to the rapid dissolution of the plasma-generated bulk WO_3, followed by the slower removal of the interfacial suboxide layer. Subsequently, the process reached a steady-state regime characterized by trace residual oxide coverage and a background etch driven by simultaneous reoxidation and metal dissolution. Although the background contribution is low, the removal step is halted before its onset to ensure controlled and selective material removal. These results were complemented by post operando X-ray photoelectron spectroscopy (XPS), transmission electron microscopy (TEM) and conductive atomic force microscopy (C-AFM) measurements. An etch rate of 8 Å/cycle was achieved and validated on both blanket and patterned films deposited by physical vapor deposition (PVD) and atomic layer deposition (ALD) using industrial-scale equipment. This demonstrates the lab-to-fab scalability of the process, thereby enabling angstrom-level precision for advanced semiconductor manufacturing.

1. Introduction

Tungsten (W) is a well-known material in the semiconductor industry due to its excellent electrical conductivity and low electromigration [1]. It is principally used in interconnects for lines, vias and plugs [2,3]. For example, in dynamic access random memory (DRAM), tungsten is used for word line and contact, whilst in NAND flash memory also as a metal gate and contact [4,5]. As industry evolves, new applications for tungsten are emerging, e.g., in magnetoresistive random-access memory (MRAM) and spintronics. In these applications, tungsten is used to ameliorate the annealing stability and the magnetic properties of magnetic tunnel junctions [6–8].

As device dimensions continue to shrink, reaching atomic scales, the complexity at the material and architecture level is increasing [9]. At these dimensions, the etching requirements become more stringent, demanding angstrom-level control, high selectivity and low surface roughness. These parameters are crucial as at such small scales, even minor deviations can have substantial impact on the device performance [10,11]. Atomic layer etching (ALE) and atomic layer cleaning (ALC) are being extensively studied for device processing, as they use self-limiting modification and removal steps, which means that the surface reactions slow down or stop as a function of time or species dosages, allowing a layer-by-layer etch with high control and uniformity [11–14].

To date, ALE is mostly based on plasma or thermal processes [15–18]. The main difference relies on the removal mechanism of the modified layers. In plasma ALE, removal occurs through the impact of energetic neutral species or ions, while in thermal ALE it is promoted by thermal energy. However, both methods present inherent drawbacks. Plasma-based processing is well known to induce physical damage (amorphization) to the substrate by plasma-generated ions [11,19]. In addition, the employed chemistry can have an impact on the properties of the material itself, and consequently, on the device properties. More specifically, halogen-based plasmas are widely used. However, due to the high diffusivity of the etching chemistry (e.g. fluorine and chlorine)

* Corresponding author at: Department of Chemistry, Katholieke Universiteit Leuven, Celestijnenlaan 200F, Leuven 3000, Belgium.
E-mail address: cinzia.chan@imec.be (C. Chan).

https://doi.org/10.1016/j.apsusc.2025.164983
Received 28 June 2025; Received in revised form 11 October 2025; Accepted 21 October 2025
Available online 24 October 2025
0169-4332/© 2025 The Author(s). Published by Elsevier B.V. This is an open access article under the CC BY license (http://creativecommons.org/licenses/by/4.0/).

material properties may be altered [20]. For example, Altieri et al. showed the impact of chlorine plasma on the magnetic properties of the ferromagnetic CoFeB alloy [21]. Thermal ALE instead often relies on halogen gas or plasma at high processing temperatures, which can further increase the diffusivity of the reagents, causing adverse effects. In the case of tungsten, thermal ALE processes typically operate at temperatures above 200°C. These approaches rely on oxidation using O_2 or O_3, followed by removal using halogen-containing precursors such as WCl_6 and WF_6 [22,23], or on more complex oxidation-conversion-fluorination sequence using cycles of O_2/O_3, BCl_3 and HF [24]. Alternative low temperature dry ALEs have also been reported, using CH_2F_2/O_2/Ar plasma and IR heating [25], or were based on fluorine radicals and oxygen ion beam [26]. Although etch rates could be well controlled in the range of 0.2 to 1.3 nm/cycle, some of these methods reported issues related to fluorine adsorption or diffusion into the underlying material.

As an alternative, wet-ALE offers isotropic removal at low temperatures without inducing physical damage or chemical modification of the underlying material. This advantage relies on the different reactivity of the ions and/or molecules in wet-chemical solutions that are stabilized by the solvent (e.g. hydration by water molecules). By consequence, these species are less reactive than radicals, ions and molecules in the gas phase, as solvation effects inherently limit mobility and diffusion of active species. However, implementation of a wet-ALE process relies on two fundamental steps: oxidation of the material surface and selective removal of the modified layer by the etchant. For polycrystalline materials, this poses challenges in preserving surface morphology, since grain-boundaries and random crystal orientations exhibit different chemical reactivity, potentially leading to local roughening [27–29]. Moreover, favorable oxide solubility during the wet oxidation step and/or chemical instability of the bare surface can hinder the process of self-limitation in wet-ALE or related (photo)electrochemical ALE processes [30–32]. Nevertheless, wet-ALE processing has been successfully demonstrated for InAs and InGaAs, and implemented at fab scale for III-V FinFET and gate-all-around device fabrication [33–35].

Determining the degree of self-limitation and selectivity in ALE processes requires high-resolution metrology sensitive to sub-monolayer etching kinetics. While X-ray reflectivity (XRR) and ellipsometry are widely used for thin-film thickness measurements, both rely on complex model fitting that introduces uncertainty at sub-monolayer resolution. More direct methods include atomic force microscopy (AFM) [36] and profilometry [26], which provide physical height measurements but lack sub-nanometer resolution and require reference masking to generate measurable step heights, thereby complicating sample preparation. Alternatively, nanogram mass changes can be monitored by quartz crystal microbalance (QCM) and converted to thickness by assuming a density [17]. However, this approach requires direct film deposition onto the QCM sensor and highly controlled environmental conditions [37,38], necessitating specialized instrumentation. In contrast, inductively coupled plasma mass spectrometry (ICP-MS) provides direct elemental quantification of the material removed from the substrate, down to picogram-level sensitivity in wet-chemical solutions. This corresponds to areal densities of the etched surface (n_{etch}) down to $\sim 1 \times 10^9$ at·cm^{-2}, making ICP-MS exceptionally well suited for quantifying angstrom-scale etching processes [33,39–42].

In this work we leverage ICP-MS quantification capability to demonstrate that oxidation of tungsten in aqueous solution is not self-limiting, as no passivating oxide forms. This inherently precludes the feasibility of a fully self-limiting wet-ALE process for this transition metal, necessitating instead a dry oxidation step based on O_2 plasma. ICP-MS kinetic studies in HCl solutions, supported by *post operando* XPS analysis, showed that the plasma-generated bulk WO_3 is rapidly dissolved, followed by the gradual removal of the interfacial suboxide layer. Once this layer is thinned, continuous oxidation and dissolution of the underlying metal occur, leading to a steady-state condition in which oxidation states persist at the surface. Based on these observations, we propose a dry-wet quasi-ALE (Q-ALE) approach. This method combines a self-limiting oxidation step using O_2 plasma with a timed oxide removal step in HCl solution at room temperature, thereby kinetically suppressing undesired etching of the underlying metal. Conductive AFM (C-AFM) and transmission electron microscopy (TEM) measurements are used to confirm the removal of the oxide while also giving additional information on surface morphology and material structure, such as distinguishing between polycrystalline and amorphous phases. Finally, lab-to-fab scalability is demonstrated on both blanket and patterned wafers with high reproducibility, underscoring the robustness of the developed process and methodologies. Therefore, the proposed dry-wet Q-ALE approach for tungsten offers an attractive alternative to current dry ALE techniques, particularly for applications that require low-temperature processing and halogen-free gas chemistries.

2. Results and discussion

In this work we discuss the process of ALE that relies on two sequential self-limiting steps: a surface modification step (e.g. oxidation), followed by the removal of the modified layer. An “ideal” ALE process is characterized by a negligible etch rate during the oxidation step, followed by a removal step in which the etch rate decreases to a level below that of significant etching of the bare material surface [13]. Here, we first investigate the role of the oxidation environment (aqueous versus gas-phase) in controlling tungsten oxidation, with the aim of achieving self-limiting oxide formation. Wet-chemical oxidation in H_2O was studied using ICP-MS to quantify dissolution kinetics, while ex situ O_2 plasma oxidation was characterized by x-ray reflectivity (XRR). The subsequent wet-chemical etching kinetics and selectivity of surface oxide removal were evaluated using electrochemical measurements and ICP-MS. *Post-operando* XPS was applied to further characterize the surface chemistry of the ALE process, while conductive AFM (C-AFM) was used to assess the uniformity of oxide removal and resulting surface morphology. Based on the characterization results, the chemistry of the W Q-ALE process is discussed and an industrial relevant process design proposed. Last, the scalability and conformality of the dry-wet Q-ALE was verified in the imec pilot line using 300 mm patterned device wafers.

2.1. *Self-limiting oxide growth for W*

Fig. 1 shows ICP-MS results for W samples immersed in 8 ppm O_3/H_2O. The areal density of the etched surface (n_{etch}) is given as a function of immersion time. Prior to each measurement, a controlled surface conditioning step was applied (see experimental section). When the sample was immersed in the O_3/H_2O solution, n_{etch} showed a linear increase in time, with an etch rate of 1.3×10^{15} at.cm^{-2} min^{-1}. This

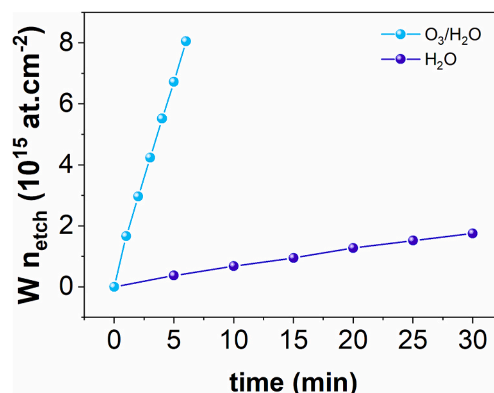

Fig. 1. Etched surface concentrations of W as a function of immersion time in 8 ppm O_3/H_2O and H_2O measured by ICP-MS. Both samples underwent surface conditioning prior to the experiment.

corresponds to 2.2 Å min^{-1} based on a density of 17.70 g/cm^3 for the PVD tungsten layer. The linear increase of the W loss in time indicates that a steady-state etching condition was reached wherein the metal is continuously oxidized and dissolved. By contrast, when the transition metal was exposed to only H_2O, the etch rate dramatically decreased to 5.8×10^{13} at.cm^{-2} min^{-1}, a difference of two orders of magnitude as compared to the O_3/H_2O solution. This result highlights the crucial role of the oxidizing agent in the wet oxidation process, while also showing that the instability of the metal in water contributes as well to the overall etching behavior (see section 2.2).

It is well known that W oxides convert to soluble WO_4^{2-} species in aqueous solution, especially for aqueous solutions with a pH > 4 [43]. Consequently, the oxide layer does not provide a stable, passivated surface in ozonated water, which is essential for achieving a self-limiting reaction during wet-ALE processing. This indicates that a dry oxidation step is required, consistent with previous tungsten ALE studies where self-limitation was achieved by O_2 or O_3 at elevated temperatures [22,24]. Furthermore, molecular dynamics simulations suggest that self-limiting oxide growth can be obtained when tungsten is irradiated by oxygen plasma [44]. In this work, the latter was adopted to achieve self-limiting oxidation.

Fig. 2 shows the tungsten oxide thickness as a function of O_2 plasma exposure time as obtained from XRR measurements and model fitting. The self-limiting nature of O_2 plasma oxidation is evident from the oxide growth kinetics: after 30 s, the oxide layer was fully formed, with no significant change in thickness with extended exposure. These results confirm the suitability of O_2 plasma oxidation for ALE processing. The oxidation rate and the oxide thickness mainly depend on temperature, oxygen partial pressure and the energy of the impacting O atoms [44–47]. The oxide thickness can, therefore, be tuned through these parameters as demonstrated by Xu et al. [48]. To further investigate the concept of the dry-wet ALE process, the plasma oxidation parameters were kept constant, and the exposure time was fixed at 90 s to ensure full saturation of oxide growth. This duration was selected for experimental consistency rather than an optimized oxidation time. Under these reference conditions an oxide layer of ~3 nm thick is obtained.

2.2. Oxide removal in HCl solution

The kinetics of the O_2 plasma oxide removal were studied for different HCl concentrations. As a strong acid, HCl dissociates into H^+ and Cl^- ions. Insight into the role of these ionic species was achieved by open-circuit potential (OCP) measurements. This surface sensitive method allows to track qualitative changes in surface chemistry as indicated by the potential response of the working electrode with respect to a known reference [49,50]. Two sets of experiments were conducted. First, the HCl concentration was varied from 0.001 to 1 M.

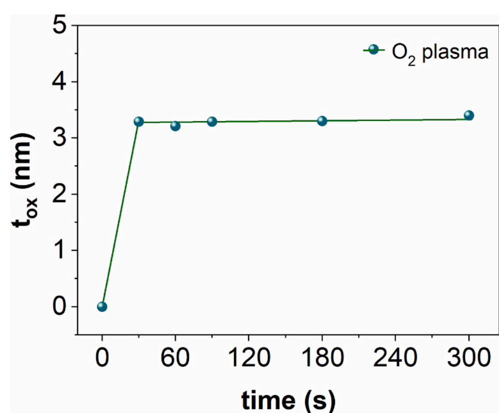

Fig. 2. XRR fitting results for the W oxide thickness versus O_2 plasma oxidation time.

The corresponding OCP measurements are shown in Fig. 3(a, top). The plots were normalized for clarity. The OCP showed a rapid response for the sample etched in 1 M HCl solution. The prominent change in surface potential occurred mostly during the first minutes of etching. The system subsequently progressed to a (quasi) steady state, achieved after around 10 min of immersion.

At lower HCl concentrations, the OCP response exhibited an increasing delay with decreasing HCl concentration. This indicates that the oxide dissolution rate lowered as the acid concentration was reduced (Fig. 3(a, top)). To decide on the importance of protons versus anions, [Cl^-] was kept constant at 1 M through the addition of KCl, while the H^+ concentration was varied (Fig. 3(a, bottom)). The OCP measurements showed a similar trend (compare Fig. 3(a) top and bottom). This suggests that the tungsten oxide dissolution is primarily controlled by the proton concentration. This is consistent with previous studies that have also highlighted the critical role of protons in the dissolution of anodic oxides, while ruling out significant contributions from various anions such as chloride, sulphate and phosphate [51,52].

To complement the OCP results, we used ICP-MS measurements to quantify the influence of the H^+ concentration on the W oxide removal rate (Fig. 3(b)). For these experiments the plasma oxidized samples were immersed for 2 min in the acid. Within this timeframe, the OCP measurements indicate that the oxide was not fully removed for any of the concentrations used and a steady state etch rate condition was not achieved. In the range 3 M > [H^+] ≥ 10^{-3} M, the etched surface density decreased with decreasing proton concentration from 3.4×10^{15} at.cm^{-2} to 1.0×10^{15} at.cm^{-2} (Fig. 3(c)). For the range 10^{-3} M ≥ [H^+] > 10^{-5} M, n_{etch} increased with decreasing proton concentration from 1.0 $\times 10^{15}$ at.cm^{-2} to 2.1×10^{15} at.cm^{-2}. This trend is consistent with anodic etching results from Anik et al. [53]. Their results showed that the steady-state current density during potential-step measurements decreased with increasing pH in the range of 0 to 2.6, reaching a minimum at pH 2.6. The minimum current density indicates that the solubility of the oxide is lowest at this pH value (i.e. optimum passivation conditions) and this was attributed to the point of zero charge (PZC) of the oxide, where etching is primarily driven by water molecules [52–54]. Towards the alkaline range, the passivation properties further deteriorated due to active etching by OH^- ions [43,53].

Based on these wet-etching results for the plasma oxide, 1 M HCl was selected as the primary etchant in this work, due to the favorable removal kinetics. Fig. 3(c) shows the relative etch rate (v_{etch}) of the oxidized W surface for 1 M HCl as a function of immersion time. The v_{etch} decreased rapidly from 1.3×10^{15} at.$cm^{-2}min^{-1}$ (2.2 Å.min^{-1}) during the first 2 min to below 9.6×10^{13} at.$cm^{-2}min^{-1}$ (0.2 Å.min^{-1}) after 10 min of immersion. This observed trend agrees well with the OCP measurements shown in Fig. 3(a). Interestingly, an additional 50 min of immersion is required to reach the background etch rate of the metal surface: 1.8×10^{13} at.$cm^{-2}min^{-1}$ (see inset Fig. 3(c)). These wet etching features can be separated into distinct stages. Initially, the bulk oxide is removed, followed by gradual dissolution of suboxides. Once a critical oxide thickness (t_c) is reached, an additional competing mechanism emerges: a background etch process driven by the continuous oxidation and dissolution of the metal in solution. This process ultimately establishes a steady-state condition in which the metal oxidation-dissolution pathway dominates the overall etching behavior. The etching dynamics can be analyzed by comparing the oxide thickness (t_{ox}) relative to t_c, as indicated in Fig. 3(c) inset. When $t_{ox} > t_c$, the process is primarily controlled by the dissolution of the oxide layer. When $t_{ox} \approx t_c$, both oxide dissolution and metal oxidation/dissolution contribute to the overall etch rate. Conversely, when $t_{ox} < t_c$, the background etch becomes the dominant factor governing the removal dynamics.

To obtain further insight into the background contribution to the overall etching kinetics, the role of dissolved O_2 in solution was investigated. Prior to the experiment, the samples were pre-etched in 1 M HCl for 20 min to ensure that $t_{ox} \leq t_c$. The results are summarized in Fig. 3 (d). For the reference case (1 M HCl without purge), the etch rate

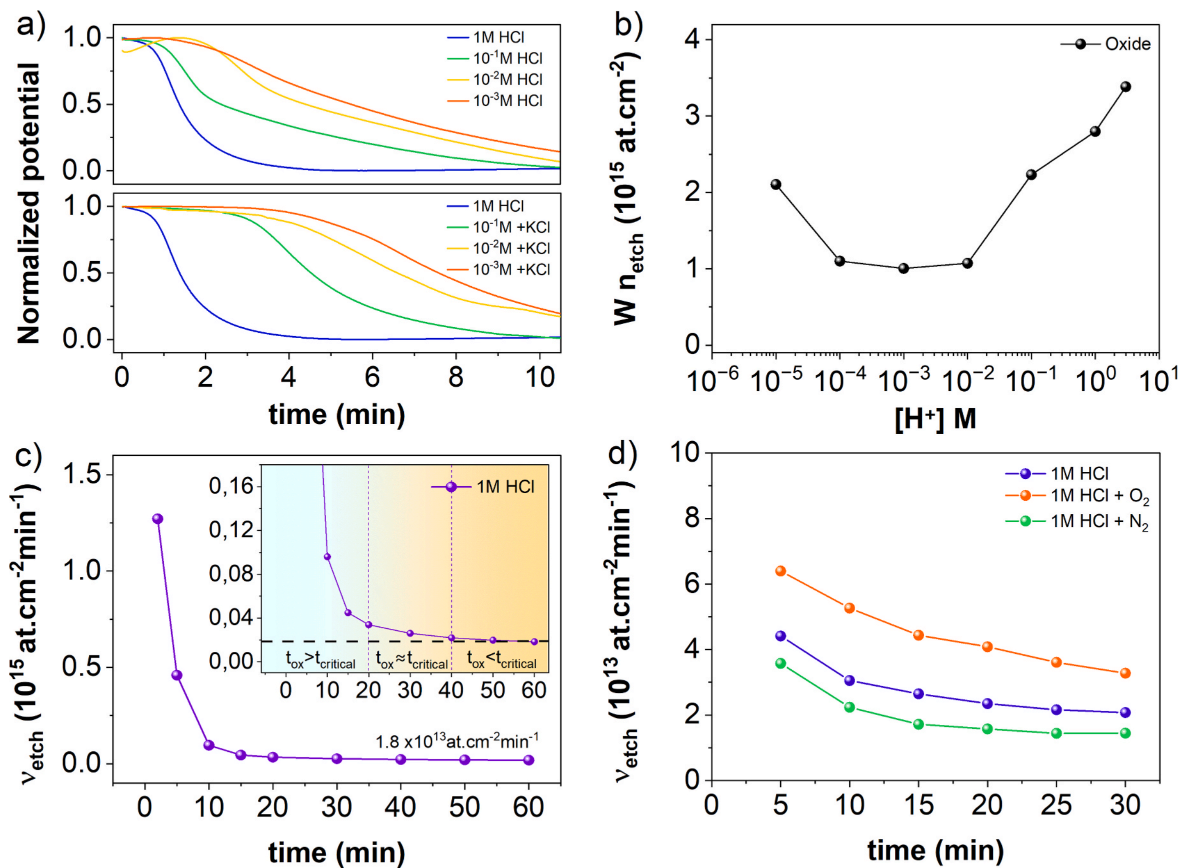

Fig. 3. (a) OCP measurements for different HCl concentrations (top) and results for varying H^+ concentration with $[Cl^-]$ fixed at 1 M (bottom); (b) Areal density of the etched W surface versus proton concentration measured by ICP-MS. The samples were etched for 2 min; (c) ICP-MS relative etch rates for the modified W surface in 1 M HCl. The insert shows a magnified view. (d) ICP-MS results showing the influence of O_2 and N_2 purging on the W etch rate as a function of immersion time in 1 M HCl solution. The W samples were pre-etched for 20 min in 1 M HCl. Note the different scale as compared to (c).

decreased to a plateau value of 2.0 × 10^{13} at.cm^{-2}min^{-1} after an additional immersion of 30 min in the solution, consistent with the behavior shown in Fig. 3(c). When the solution was saturated with O_2, the etch rate increased approximately twofold, to 4.0 × 10^{13} at.cm^{-2}min^{-1} as compared to the reference. Conversely, purging the HCl with N_2 reduced the background etch rate to 1.5 × 10^{13} at.cm^{-2} min^{-1}. These results demonstrate that when $t_{ox} \leq t_c$, oxidants can reach the metal surface and induce etching. The etch rate of the metal in this regime is controlled by the oxidant concentration as well as the oxide removal kinetics. In Section 2.3 we show that bare metal oxidation proceeds through intermediate steps that involve suboxide formation as demonstrated by XPS.

When the sum of n_{etch} is plotted as a function of immersion time in 1 M HCl (Fig. 4(a)) instead of the v_{etch} (Fig. 3(c)), insight into the oxide removal kinetics is provided for the different stages of etching as well the thickness of the oxidized W layer. A sharp increase is observed for n_{etch} during the first 5 min of immersion in the etchant with a removal of 2.6 × 10^{15} at.cm^{-2} and 4.0 × 10^{15} at.cm^{-2} for 2 and 5 min, respectively. For longer immersion times, the removal rate lowers, and the total amount of etched W species reaches 4.8 × 10^{15} at.cm^{-2} after 20 min of immersion, which corresponds to ~95 % of the W that was oxidized by the O_2 plasma (~8.3 Å of metal that was converted to oxide). Using the reported W-to-WO_3 expansion factor of 3.3 [55], this amounts to an oxide thickness of ~2.7 nm, in good agreement with our TEM results (see section 2.4).

During the following 40 min of immersion, an additional loss of 8.6 × 10^{14} at.cm^{-2} was measured (1.4 Å of W converted to oxide). At this stage, n_{etch} cannot be attributed solely to the removal of the plasma-grown oxide, as the background etch rate of the metal becomes significant.

The decreasing etch rate towards the suboxide interface (Fig. 3(c)) indicates that the oxide-to-metal etching selectivity decreases with increasing immersion time. For the regime where $t_{ox} > t_c$, the selectivity was ~70 relative to the background etch rate but decreased to ~2 as the oxide thickness approached the critical thickness (t_c). The results in Fig. 4(a) indicate that t_c is reached when approximately 95 % of the oxide was removed. The remaining 5 % residual oxide corresponds to a~ 0.4 Å thick W layer that is converted to suboxide (see XPS results). For the regime $t_{ox} < t_c$ the selectivity gradually decreased to unity as the suboxide was completely removed (after 50 min of etching). We note that the apparent oxide-to-metal selectivity of ~70 is likely a lower bound, since the background metal dissolution rate (0.03 Å min^{-1}) becomes negligible once the surface is fully covered by oxide. Under such conditions, charge transfer to the electrolyte is effectively blocked, and the true selectivity is expected to be considerably higher (see also section 2.5).

Fig. 4(b) shows ICP-MS quantification results for 5 consecutive ALE cycles. In this case, the O_2 plasma oxidation was performed in a laboratory setup rather than on the 300 mm production tool used for the other experiments (see in experimental Section 4). Despite this deviation in oxide growth condition, the ALE process exhibited excellent reproducibility when the oxide-removal step was confined to the $t_{ox} \approx t_c$ regime, yielding a n_{etch} of 4.7 ± 0.2 × 10^{15} at.cm^{-2}.

2.3. Surface and interface composition analysis

To further corroborate the ICP-MS findings described in the previous section, complementary surface chemical composition analyses were

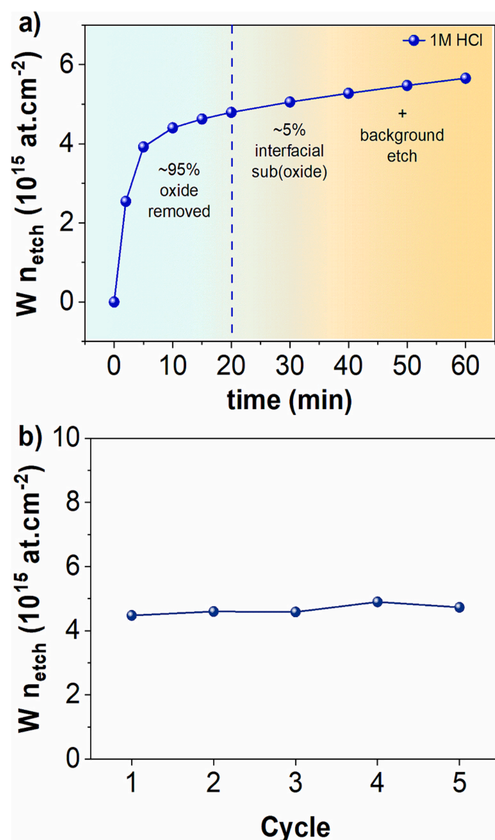

Fig. 4. (a) Total W surface areal density in function of immersion time in 1 M HCl. (b) Quantification results for 5 ALE cycles: 1 cycle involves 90s plasma O_2 oxidation followed by 20 mins of oxide removal in 1 M HCl solution.

conducted. To exclude controversial ambient effects, samples were prepared *in situ* in a dedicated wet-chemical chamber connected to the Daisy FUN XPS set up of the TU Darmstadt [56]. Fig. 5 presents the W 4f spectra fitted with 4 doublet peaks with a spin–orbit splitting of 2.2 eV. The reference spectrum, after O_2 plasma oxidation, showed a prominent W^{6+} oxidation state (BE 36.1 eV) next to the W^0 metal peak at a binding energy (BE) of 31.6 eV. The $W_{5p3/2}$ loss peak was positioned at 37.4 eV [57,58]. A small contribution of W^{5+} (BE 34.6 eV) and W^{4+} at 32.2 eV were also observed [58,59]. These peak fittings indicate that the bulk of the plasma oxide consists of WO_3. This is further confirmed by the O 1s spectra in Fig. 6, which presents a prominent peak at 531.0 eV attributed to the oxygen in WO_3, and as well a peak at 530.5 eV for the suboxides (WO_{3-x}) [60]. The peaks found at 532.0 and 533.1 eV are related to

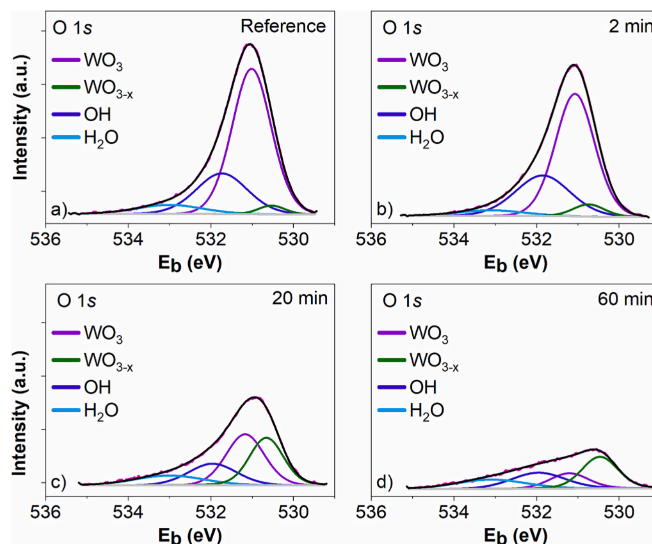

Fig. 6. Post operando XPS spectra of O1s. (a) Reference sample after plasma O_2 oxidation, and after etching in 1 M HCl for 2, 20 and 60 min (b-d).

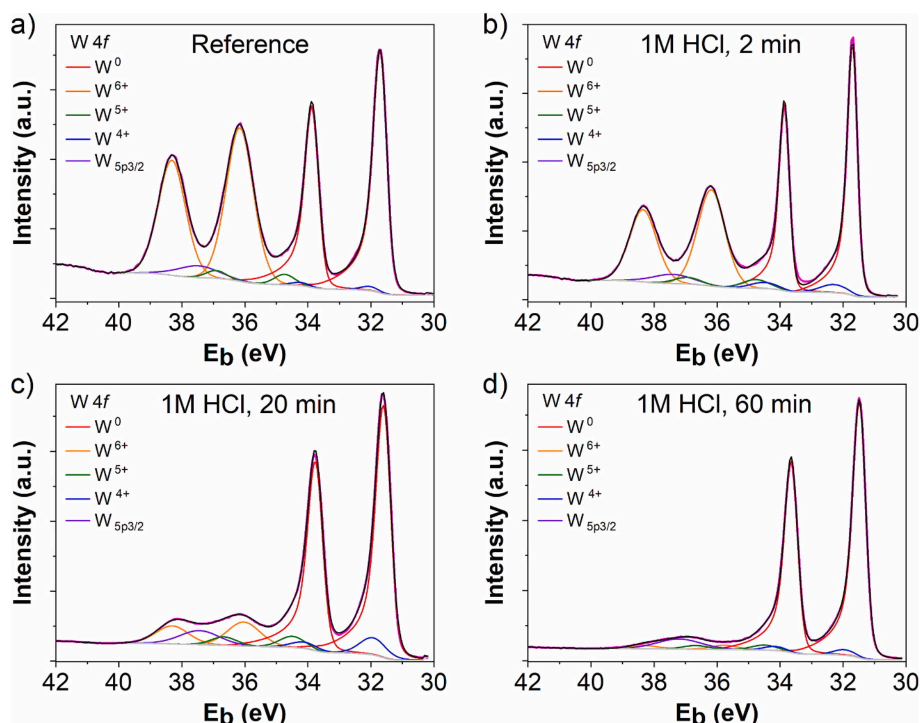

Fig. 5. Post operando XPS spectra of W 4f. (a) Reference sample after plasma O_2 oxidation, and after etching in 1 M HCl for 2, 20 and 60 min (b-d).

hydroxide (with possibly some contribution of C-O) and adsorbed H_2O species, respectively [60–62].

When the sample was etched for 2 min in 1 M HCl, the W^{6+} feature was readily lowered while after 20 min of immersion most of the bulk WO_3 was removed (Fig. 5(b and c)), as also indicated by the ICP-MS measurements (Fig. 4(a)). As a result, the suboxides (W^{5+} and W^{4+}) at the interface between WO_3 and the metal are exposed at the outer surface, explaining their increased atomic percentages from XPS. This trend is in good agreement with the O 1s spectra in Fig. 6(a–d). These suboxides exhibited a very low etch rate (Fig. 4(a)), indicating their intrinsic chemical stability, and suggesting that dissolution requires prior oxidation to higher oxidation states. Moreover, the persistence of these species, together with W^{6+} detected in small atomic percentages even after 60 min of etching, points to their continuous formation during steady state conditions. Since W lies outside the electrochemical stability window of H_2O, achieving an oxide-free surface in aqueous etchants may not be feasible. In such cases, solvent-based etchants and strictly controlled oxygen-free environments may be required. The atomic percentages calculated from the relative peak areas of W 4f are summarized in Fig. 7. These reflect the same trends we observe in O 1s for WO_3 and $WO_{3\text{-}x}$. The comprehensive atomic percentages of W 4f and O 1s are reported in Table S1.

Some surface chlorides were detected during etching of bulk WO_3, which may point to the formation of oxychloride species (Fig. S1). However, the OCP measurements did not reveal a clear impact of Cl^- on the removal rate of WO_3. The Cl 2p signal may also partly originate from the drying process in the preparation chamber, as no water rinse was applied. After 60 min of immersion, the Cl 2p peak was negligible, suggesting that any chloride-related species are either unstable under these conditions or below detection limit.

The oxide thickness was approximated from XPS atomic percentages, using TEM results as reference (see next section). Although ICP-MS and XPS are complementary characterization techniques, the atomic concentrations derived from the fitted XPS spectra show a discrepancy when compared to the ICP-MS quantification results (Fig. 4(a)). In the latter case, the thickness of the removed oxide layer amounted to 1.4 nm and 2.7 nm, for 2 min and 20 mins respectively. In contrast, the XPS results indicate respective values of 0.5 nm and 2.1 nm. This inconsistency may originate from the XPS fitting procedure, although sample preparation could also play a role. For ICP-MS analysis, the solution is dispensed across the sample surface, promoting convective mixing and diffusion effects. While oxide dissolution is primarily kinetically controlled, diffusion effects cannot be fully excluded [54,63]. This is supported by experiments that showed that the etched surface density increased by 25 % when the sample rotation rate was increased from 0 to 500 rpm (Fig. S2). In contrast, the in-situ wet-chemical cell used for XPS constrains the etchant volume, requiring the use of a static droplet carefully positioned on the sample surface under inert ambient conditions.

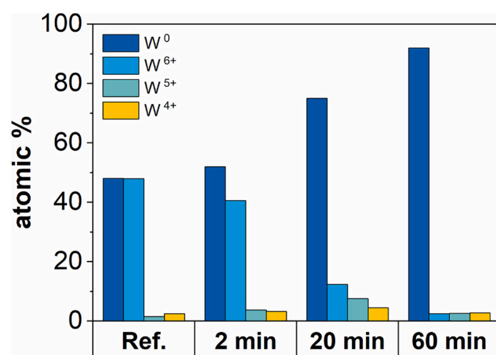

Fig. 7. Atomic percentages for W^0, W^{6+}, W^{5+} and W^{4+} in W 4f obtained from the XPS fittings for the reference sample and after 2, 20 and 60 min of etching in 1 M HCl.

2.4. Surface morphology characterization

AFM and C-AFM measurements were performed to assess the uniformity of the plasma oxidation combined with the wet etching step. Plasma oxidation reduced the average roughness of the as-deposited tungsten film from 0.32 nm to 0.12 nm (compare Fig. S3 with Fig. 8 (a)), resulting in a smoother surface.

The surface roughness remained constant at ~0.1 nm during 60 min of immersion in 1 M HCl (Fig. 8(a–d)), supporting the high chemical stability of the exposed metal surface towards the acid. The etching proceeded uniformly, without evidence of preferential attack at grain boundary or other defect-related sites once the oxide was removed (Fig. 8(d)). The average conductivity of the layer increased over time consistent with oxide removal (Fig. 8(e–h)). The oxide recess was, however, not fully uniform in time as indicated by the conductivity map. This indicates some local variations in oxide density and or quality across the thin film.

More information about the structural and morphological characteristics of the metal and the oxide was obtained by transmission electron microscopy (TEM), high-angle annular dark-field scanning transmission electron microscopy (HAADF-STEM) imaging and energy-dispersive X-ray spectroscopy (EDS). The results in Fig. 9 show that the PVD W layer is polycrystalline, while the plasma oxide is amorphous, with a thickness of about 2.5 ± 0.2 nm. The metal/oxide interface is smooth. In the HAADF mode, the oxide and metal layer are well distinguishable highlighted by the STEM-EDS results where tungsten and oxygen are indicated (Fig. 9(c and d)). ICP-MS quantification showed that ~0.8 nm of metallic tungsten was converted into oxide, which gives an oxide expansion factor of 3.3 when compared to the oxide thickness measured by TEM. This is in good agreement with findings reported in literature [55]. On the other hand, the XRR data fitting yielded a thickness value 27 % higher than that measured by ICP-MS and TEM. The reason for this relatively large discrepancy between the (indirect) XRR fitting results and the direct quantification methods is not clear. One possible explanation is the fitting complexity of the multilayer stack, which may contribute to the overestimation of the oxide thickness. This hypothesis is further supported by the extracted XRR density for the oxide layer of 5.4 $g.cm^{-3}$, which is lower than the 7.4 $g.cm^{-3}$ value derived from ICP-MS and TEM measurements (see more fitting details in experimental section 4).

Fig. 9(e–h) shows the TEM results for the plasma oxidized sample after 20 min of immersion in 1 M HCl. Following the wet etching step, which removes ~95 % of the oxide (Fig. 4(a)), the clear distinction between the oxide and the metal layer is no longer visible. However, EDS mapping still indicates a thin layer of W-O (Fig. 9(g and h)) on top of the sample, even though no contrast between the two layers is observed in the HAADF image. This residual oxide may originate from uncontrolled reoxidation during the ex-situ sample preparation.

2.5. Tungsten dry-wet Quasi-ALE chemistry and process design

In the previous sections, we have shown that a wet-ALE process is not feasible for tungsten, due to the formation of unstable tungsten oxides in O_3/H_2O solution. In contrast, O_2 plasma produces a self-limiting oxide layer and is therefore adopted as the metal modification step in the proposed ALE process. Our XPS results show that exposure of the metal surface to O_2 plasma results in the formation of an oxide layer primarily composed of WO_3, with suboxides present at the metal interface. These findings are consistent with previous molecular dynamics simulation studies by Sharkass et al. [44], which showed that during oxygen bombardment of the surface, O atoms migrate towards the bulk while W atoms diffuse towards the surface, leading to a saturation thickness. In their simulations, the outer layers of the oxide reach an O:W atomic ratio of 3:1, which then decreases in the transitional boundary region between bulk metal and oxide and progressively approaches zero deeper into the bulk. Although the simulations were conducted at room

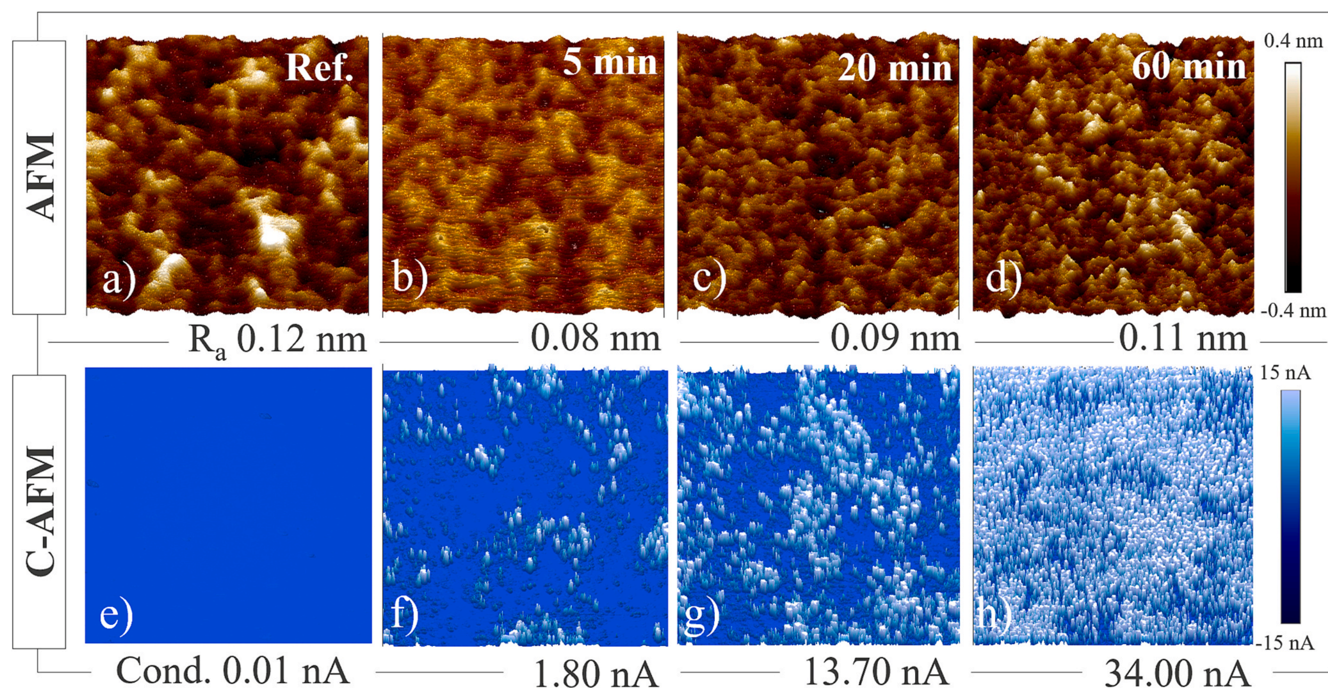

Fig. 8. (a-d) Tilted AFM images of unetched sample and after 5, 20 and 60 min of etching in 1 M HCl. Value scale −0.4 to 0.4 nm. (e-h) Corresponding tilted C-AFM images with current value scale ranging from −15 to 15nA. Scan size for all the samples was 1x1 μm^2.

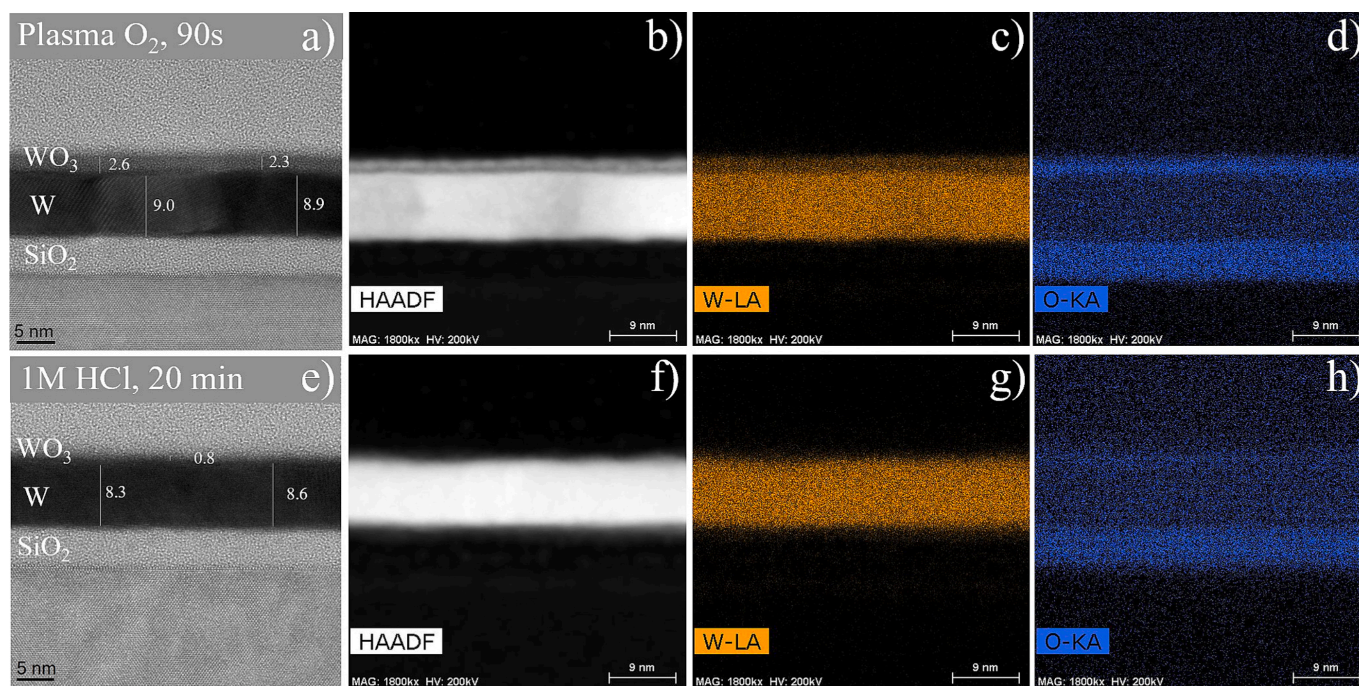

Fig. 9. TEM of oxidized samples before (a-d), and after an etch of 20 min in 1 M HCl (e-h).

temperature and our experiments at 60̊C, the proposed oxidation mechanism is in good agreement with our observations.

Following the metal oxidation step, the oxide removal was investigated for different HCl solutions using electrochemical measurements and ICP-MS. These results indicate that oxide dissolution primarily depends on protons while the effect of chloride ions was negligible. A 1 M concentration was selected to ensure favorable etching kinetics. Oxide dissolution is characterized by distinct etching regimes. The first corresponds to the removal of bulk WO_3 when the oxide thickness exceeds the critical thickness ($t_{ox} > t_c$). In this regime, the outer WO_3 layer is attacked by protons that convert the trioxide into soluble WO_2OH^+ and WO_2^{2+} species [53,54,64,65]. This is described by the following reactions:

$$WO_{3(s)} + H^+ \rightarrow WO_2OH^+_{(aq)} \quad (1)$$

$$WO_2OH^+_{(aq)} + H^+ \leftrightarrows WO^{2+}_{2(aq)} + H_2O \quad (2)$$

Water molecules may also contribute to oxide dissolution, though to

a lesser extent than protons at pH 0 [53]. This pathway involves an intermediate hydration of the dry oxide prior to release of tungstic acid from the surface:

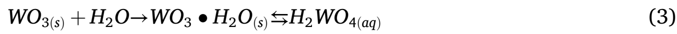

$$WO_{3(s)} + H_2O \rightarrow WO_3 \bullet H_2O_{(s)} \leftrightarrows H_2WO_{4(aq)} \quad (3)$$

The formation of polytungstates during the etching of tungsten is well established and generally expected for acidic solutions when W concentrations exceed 0.01 M [66,67]. However, during the experimental conditions used in this work, the maximum concentration was $\sim 10^{-7}$ M, far below this concentration limit. Therefore, the formation of these complex tungsten species is unlikely.

When the etch front approaches the suboxide interface, the etch rate decreases. Unlike WO_3, tungsten suboxides at the metal-oxide interface exhibit significantly lower dissolution rates. Their persistence reflects the higher chemical stability of W in intermediate oxidation states (W^{4+}/W^{5+}), which require reoxidation to W^{6+} before dissolution into soluble tungstate species can occur. Consequently, suboxide dissolution is kinetically hindered and becomes the rate-limiting step as the etch front approaches the interface. When the residual oxide layer reaches the critical thickness ($t_{ox} \approx t_c$) the kinetics of suboxide dissolution and metal oxidation begin to compete. As a result, the oxide-to-metal selectivity decreases. Ultimately, the system evolves towards a steady-state condition ($t_{ox} < t_c$) in which oxidation and dissolution of tungsten occur simultaneously. This background etching process leads to a gradual metal loss of approximately 0.03 Å min^{-1}. The corresponding steady-state surface chemistry is characterized by a trace-level coverage, consisting of W^{6+}, W^{5+} and W^{4+} species, as evidenced by XPS. These oxidation states arise from electrochemical driving forces associated with oxidation by dissolved oxygen at the metal-electrolyte interface:

$$2\,W + 3\,O_2 \rightarrow 2\,WO_{3(s)} \quad (4)$$

Moreover, tungsten's relatively low work function positions its Fermi level just outside the electrochemical stability window of water:

$$W + 3\,H_2O \leftrightarrows WO_3 + 3\,H_2 \quad (5)$$

If metal oxidation were driven by the H^+/H_2 redox couple, the potential difference with the W/WO_3 equilibrium is (≈0.09 V) [68], whereas the overpotential for O_2/H_2O is much larger (≈1.32 V). These values indicate that the background etch rate is mainly governed by the presence of dissolved O_2 species. Reaction (5) can proceed through intermediate oxidation states, which explains the presence of mixed valence suboxide species in equilibrium at the interface. Locally, direct dissolution of the metal may also occur via the formation of soluble tungstate species accompanied by hydrogen evolution:

$$W + 4\,H_2O \rightarrow H_2WO_4 + 3\,H_2 \quad (6)$$

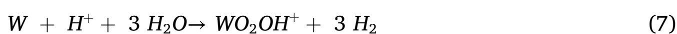

$$W + H^+ + 3\,H_2O \rightarrow WO_2OH^+ + 3\,H_2 \quad (7)$$

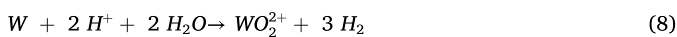

$$W + 2\,H^+ + 2\,H_2O \rightarrow WO_2^{2+} + 3\,H_2 \quad (8)$$

However, given the small overpotentials and the very low background concentrations measured by ICP-MS, these pathways are unlikely to contribute significantly to the overall etch rate. Therefore, the steady-state metal dissolution kinetics are governed by a series of coupled processes, including (i) the initial oxidation of metallic W by dissolved O_2, (ii) the conversion of suboxide species (W^{4+}/W^{5+}) to WO_3, and (iii) the dissolution of WO_3 into solution. The overall rate is determined by the slowest of these steps, with suboxide oxidation to WO_3 likely representing the rate-limiting process. Further kinetic studies will be required to quantify the relative contributions of each step.

Given the low atomic-scale etch rate in the steady-state regime, the process cannot be regarded as fully self-limiting. The observed background etch rate reveals a fundamental limitation: a completely oxide-free tungsten surface cannot be sustained in aqueous solutions. Within the Q-ALE framework, this limitation can be mitigated by confining the oxide removal step to the regime where $t_{ox} > t_c$, thereby suppressing the background etch rate and ensuring a stable metallic surface beneath the bulk oxide. After each cycle the metal remains covered with a residual oxide layer, which serves as the starting surface for the subsequent oxidation step. Owing to the self-limiting nature of tungsten plasma oxidation, a consistent oxide thickness is achieved during each cycle, while the time-controlled wet-etch step ensures a reproducible residual oxide thickness. Furthermore, the residual oxide plays a beneficial protective role, suppressing uncontrolled reoxidation during ambient exposure. Even when the oxide thickness is below the critical threshold (t_c) after removal, a 30-minute exposure to air causes only ~0.4 Å of metal reoxidation, compared to ~2.0 Å after 1200 min (Fig. S4).

Based on these insights, the dry-wet Q-ALE process is defined by a dry plasma modification step, followed by a wet removal step that is halted before $t_{ox} > t_c$. A schematic representation of this hybrid atomic-layer etching sequence is shown in Fig. 10.

For applications requiring additional thinning or further minimization of the residual oxide, a final tailored step may be introduced. This step could involve applying a higher acid concentration to enhance oxide dissolution, while reducing the oxidant concentration to suppress reoxidation. Under such conditions, a near oxide-free surface can be approached, representing the closest state to an oxide-free tungsten surface achievable within this method.

2.6. Dry-wet Quasi-ALE demonstration on large area blanket and patterned tungsten films

To demonstrate industrial relevance, the conformality and morphological impact of the dry-wet Q-ALE process were investigated on both blanket and patterned device structures, using 300 mm equipment integrated into the existing imec pilot line. The process consisted of two steps: 90 s plasma oxidation followed by a 5 min oxide removal in 1 M HCl.

Fig. 11(a and c) show SEM images of the unprocessed and the processed PVD blanket wafer after 10 Q-ALE cycles. The initial W thickness was about 20 nm, of which ~8 nm was removed, corresponding to an estimated removal rate of ~8 Å / cycle. Inline AFM imaging showed an increase in mean surface roughness (R_a) from 0.25 nm to 0.41 nm, likely due to slightly higher oxidation rate at grain boundary sites, which become apparent after significant layer recess (Fig. 11(b and d) [27]. Some residues were observed after ALE cycling, since no dedicated post-cleaning step (e.g. water rinse) was implemented in this study. Post-process cleaning will need to be optimized for improved morphology control.

The experiment was repeated for tungsten films deposited on shallow trench isolation (STI) structures, using a TiN adhesion layer. Two deposition methods were employed: PVD and ALD. Fig. 12(a and b) shows that PVD is not conformal, leading to significant thickness variations across the patterned structures. Nevertheless, the deposited film is smooth, which reflects the dense and continuous growth typical of the PVD process. The thickness varied from 4.0 nm at the bottom to 20.5 nm at the top of the features. After 10 Q-ALE cycles, the film thickness on the top STI region decreased at an average rate of ~8 Å / cycle, with no significant impact on surface roughness (Fig. 12(c and d)). In areas where the tungsten film was thin, full removal of the metal was observed. The underlying TiN adhesion layer remained intact after metal recess, demonstrating the selectivity of the Q-ALE process for tungsten while preserving the integrity of the TiN liner.

In contrast to PVD, ALD produced conformal tungsten layers on the patterned substrate, though with some surface roughness (Fig. 12(e and f)). After 10 Q-ALE cycles, the film was etched uniformly across the trench with an average etch rate of ~8 Å / cycle, while STEM-EDS mapping did not reveal any significative chlorine presence (Fig. S5). Supporting ICP-MS measurements on coupons confirmed a reproducible elemental loss of 313.5 ± 18.7 ppb/cycle (Fig. S6). The uniform etch profile shown in Fig. 12 is consistent with isotropic etching behavior, as

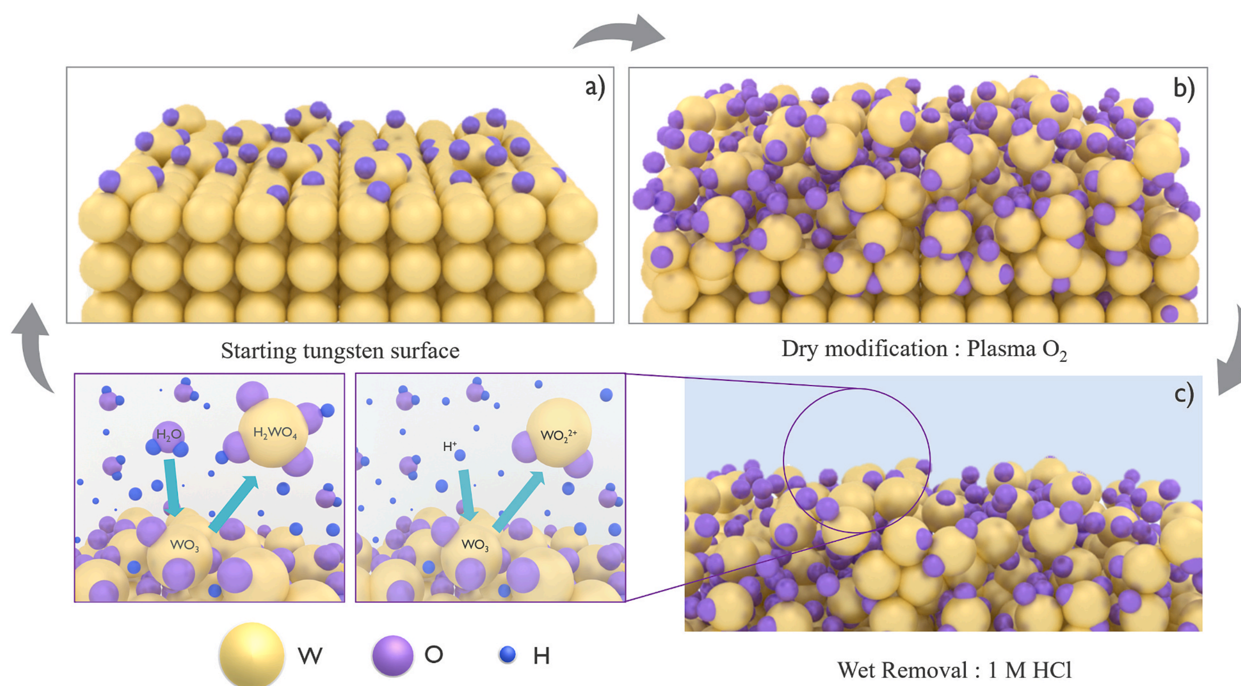

Fig. 10. Schematic dry-wet Q-ALE etching model. (a) Initial tungsten surface covered with residual suboxides. (b) Self-limiting oxidation of tungsten using O_2 plasma oxidation, forming a controlled surface oxide. (c) Selective removal of the bulk oxide in 1 M HCl, reaching the suboxide interfacial layer, which serves as a stable starting surface for the subsequent cycle.

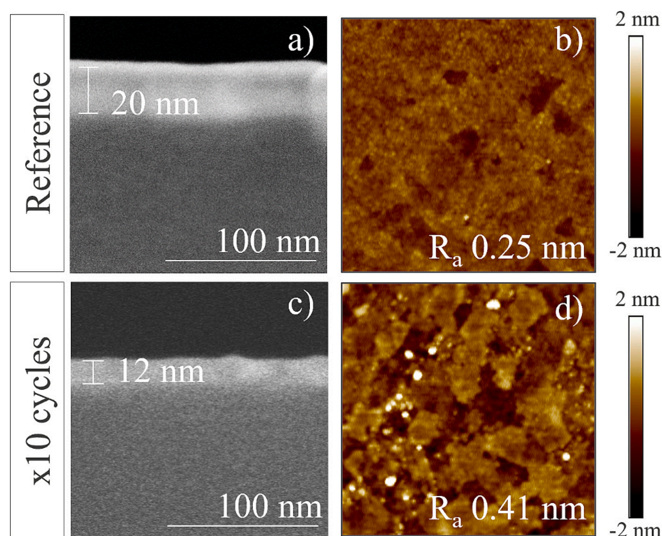

Fig. 11. Cross-section SEM and AFM of reference (top, (a, b)) and processed wafer after 10x cycles (bottom, (c, d)). AFM scale is −2 to 2 nm, while the scan size is 1x1 μm^2.

expected under these process conditions where both the plasma oxidation and wet removal steps act without pronounced directionality. It is noted that at higher aspect ratios, deviations from isotropic etching may occur due to transport limitations. ICP-MS values measured in the laboratory showed that approximately 6.8 Å of oxide was removed, in contrast to the 8 Å per cycle for the integrated Q-ALE process in the 300 mm pilot line. This deviation can be attributed to fab-level factors influencing the wet-etching step, such as wafer rotation and flow dynamics associated with etchant delivery, whereas the laboratory experiments were performed in a static etching cell. These aspects should be examined further to fully understand their impact on the etching behavior. Overall, the results indicate that the dry-wet Q-ALE process can be applied reproducibly to tungsten films prepared by different deposition methods, while maintaining oxide-to-metal selectivity and preserving surface morphology. These findings highlight the viability of the process for integration into existing manufacturing environments and toolsets.

3. Summary and conclusions

In this work, a combined dry-wet Quasi-Atomic Layer Etch (Q-ALE) process was demonstrated using tungsten as a model case. The method involves O_2 plasma modification of the metal surface to form a self-limiting WO_3 layer, followed by timed removal in 1 M HCl at room temperature. Kinetic analysis shows that oxide dissolution is predominantly proton-driven (H^+ attack). When the oxide thickness decreases to a critical value (~5% of the initial thickness), a background etching regime is entered, characterized by simultaneous reoxidation and metal dissolution. Although the background etch proceeds slowly (0.03 Å. min^{-1}), it can be avoided by halting the removal step before reaching the critical oxide thickness, thereby maintaining operation within the oxide-dissolution regime. As a result, the Q-ALE process effectively combines a self-limiting oxidation step with a time-controlled removal step governed by kinetic rather than strictly self-limiting constraints.

The process was validated through ICP-MS and XPS using *in situ* sample preparation. Complementary C-AFM and TEM analyses confirmed the removal of the amorphous oxide during the wet-etch step, yielding low roughness and good conformality. These results indicate that the grain boundary sites of the polycrystalline metal are chemically stable. However, when significant recess occurs, a slight increase in roughness was observed, possibly caused by a higher oxidation rate at grain boundaries during the modification step. The proposed dry-wet Q-ALE method was further validated on 300 mm patterned wafers using industrial processing tools, demonstrating an isotropic etch rate of about 8 Å / cycle for both tungsten PVD and ALD layers with an aspect ratio down to 1:4.

The principles of the dry-wet Q-ALE approach can be extended to other CMOS-relevant metals such as Cu and Mo. Both form slightly

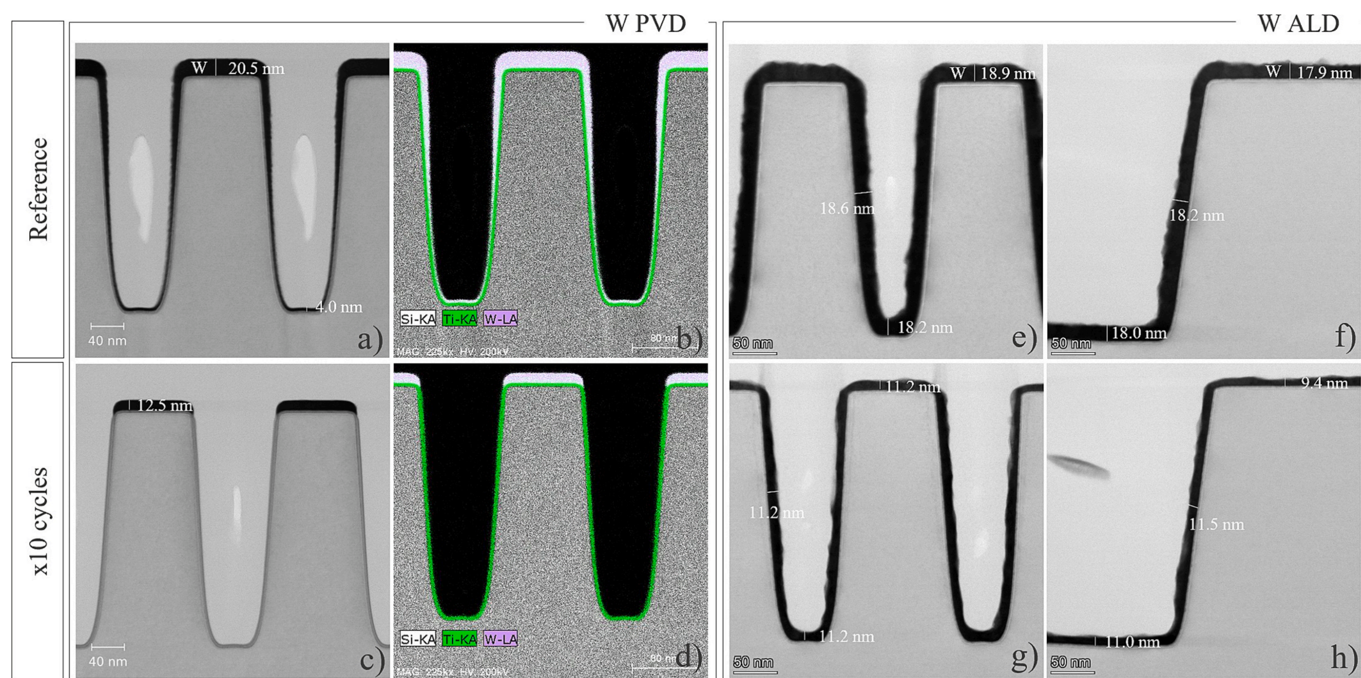

Fig. 12. Shallow trench isolation (STI) patterned wafer with PVD W before (a, b) and after 10 Q-ALE cycles (c, d) and for deposited ALD W before (e, f) and after 10 Q-ALE cycles (g, h).

soluble oxides under wet oxidation, which hinders self-limiting behavior, yet they exhibit good oxide-to-metal selectivity during the wet etching step. Noble metals such as Ru and Pt, although difficult to oxidize wet-chemically, produce oxide products that are soluble in conventional acids. For these metals, a dry oxidation step can be used to generate the surface product layers of controlled thickness.

Interestingly, classical semiconductors such as Ge and the Ga-rich group III–As and III–Sb compounds form unstable wet oxides, which prevents fully wet-ALE operation, yet they exhibit excellent oxide-to-metal selectivity during the wet-etching step. In contrast, group III nitrides are chemically stable, but their oxides dissolve readily, making them suitable for dry-wet ALE schemes. Thus, the combined dry-wet ALE framework approach provides a versatile and scalable platform for layer-by-layer etching of a broad range of technologically important materials.

Furthermore, the present findings suggest that the self-limitation reported in the literature for many processes may, in part, reflect the detection limits of conventional thickness-based metrology. The ICP-MS quantification employed in this work provides the resolution needed to detect residual background etching, offering an improved basis for assessing the degree of self-limitation and therefore more accurately distinguishing truly self-limiting behavior from apparent saturation effects.

4. Experimental section

Materials and Chemicals. W polycrystalline films with a thickness of 10 nm were deposited by Physical Vapor Deposition (PVD) sputtering by DC power using the Anelva C-7100 GT system on 300 mm wafers. The growth substrate consisted of thermally grown SiO_2, formed at 850°C on Si wafers. In-line mass measurements (Metryx, Lam Research) were performed to determine the deposited mass. Based on these measurements, a film density was calculated of 17.70 ± 0.17 g.cm^{-3} [69]. The dry metal oxidation step was carried out in an industrial Lam Research system Kiyo® with an ICP chamber with 30 mTorr chamber pressure, 600 W RF power, 480 sccm O_2, 0 V bias and substrate temperature of 60 °C.All the oxidation steps were carried out in the Lam system, except for the experiment shown in Fig. 4(b), where a PlasmaTherm APEX system (40 mT/ 500 W RF power / 230 V bias/ 150 °C / 60 s) was used.

For the wet oxidation experiments, O_3/H_2O mixtures were prepared using a MKS LIQUOZON® ozone generator that was connected to a wet bench in the ultra-clean processing lab of imec. Wet-chemical solutions were prepared from trace-grade HCl (37 %, 12 M) purchased from Sigma Aldrich and diluted with ultrapure water.

Surface preparation. Prior to each experiment the native oxide was removed by immersing the sample in 1 M HCl for 20 min. This ensures a reproducible starting surface with a controlled residual oxide thickness and minimizes the effect of uncontrolled oxidation due to storage and ambient exposure.

Etching kinetics. Experiments were conducted at room temperature in a cleanroom environment using a polytetrafluoroethylene (PTFE) etching cell with a Kalrez® O-ring, exposing 3.14 cm^2 of the sample surface to 10–20 mL HCl solution. The solution was not stirred. The etching kinetics was quantified by measuring the ^{182}W concentration in the etchant by inductively coupled plasma mass spectroscopy (ICP-MS, Thermo Fisher iCAP TQ-s) using kinetic energy discrimination in He mode. Each sample was diluted and matched to the calibration matrix, if needed. Measurement error was determined to be within 5 % with background equivalent concentrations < 1 ng L^{-1}. The thickness was calculated based on the measured W concentration by ICP-MS, using the measured tungsten metal density (17.70 g.cm^{-3}). The N_2 or O_2 purging was performed using a coiled, perforated PFA tube immersed in the etching solution. When N_2 was used, the etching cell was additionally enclosed in a small chamber with a slight N_2 overpressure to further suppress O_2 diffusion into the solution.

Open Circuit Potential (OCP) measurements were conducted using a conventional three-electrode configuration with a Pt counter electrode and an Ag/AgCl reference electrode. The geometric surface area of 0.95 cm^2 was defined by a Kalrez® O-ring mounted in a PTFE electrochemical cell. Potential measurements were conducted at room temperature using a potentiostat (Princeton Applied Research, PARSTAT 4000) computer controlled by VersaStudio software.

Surface characterization. X-ray Photoelectron Spectroscopy (XPS) data were collected at the Darmstadt Integrated System for Fundamental Research (DAISY-FUN). Samples were processed in a glass chamber directly attached to the cluster tool under argon inert atmosphere, after

which they were transferred in a buffer chamber and in the Ultra High Vacuum (UHV) system at a base pressure of $< 10^{-9}$ mbar, avoiding ambient exposure. The analysis was carried out with a SPECS PHOIBOS 150 analyzer and SPECS Focus500 X-ray source. The measurements were performed using a monochromatized photon beam of Al Kα ($h\nu = 1486.6$ eV). All measurements were collected with a 45° exit angle with a pass energy of 10 eV, with the exception of the W 4f spectrum, which was measured at a pass energy of 20 eV. This difference leads to peak broadening but does not significantly impact the reported atomic percentages, as these values are based on the ratio of the peak areas. XPS fitting was done with Voigt and Doniach-Sunjic functions with Shirley background by CasaXPS software. X-ray reflectivity (XRR) measurements were conducted on a Bruker D8 Discover with a Cu-Kα source and fitting was done through GenX [70].

The discrepancy between XRR fitting and ICP-MS and TEM results is likely due to the complexity of the multilayer stack formed by Si/SiO_2/W/WO_3. In the XRR analysis, multiple parameters i.e., thickness, density, and roughness, were fitted simultaneously (excluding the Si substrate). This inherent fitting complexity may contribute to the overestimation of the oxide thickness. Nonetheless, the figure of merit (FOM) for the fittings was always below 0.01, indicating a very good match between the fit and the experimental data.

For the C-AFM measurements, a Bruker ICON AFM was used in a glove box under controlled argon ambient. Silver paste was used to electrically contact the samples and measurements were done with an applied bias of 75 mV. Samples were measured *ex situ* and loaded within 15 min from the wet processing.

Dry-Wet Q-ALE demonstration. The 3D shallow trench insulation (STI) structures were prepared starting from blanket Si wafers, oxidized (in-situ steam generation) to obtain 5 nm SiO_2 pad oxide. Subsequently, 50 nm silicon nitride (Si_3N_4) was deposited, followed by a double sacrificial hard-mask composed of spin-on carbon (SoC) and spin-on glass (SoG). After photoresist coating, the wafers were patterned using immersion 193 nm photolithography, targeting dense and isolated trenches of 90 nm width. The wafers were then etched in a 300 mm plasma etch chamber (Lam Research Kiyo®), with a multi-step process sequence aiming first at opening the SoG and SoC, then the Si_3N_4 and the pad oxide, and finally etching the bulk silicon by means of a HBr/Cl_2-based process. After ending the silicon etch, the SoC residues were stripped in-situ by means of a N_2-O_2 plasma, while the silicon nitride hard-mask was removed by means of an H_3PO_4 − SC1(5:1:1 H_2O:H_2O_2:NH_4OH) − HF wet etch sequence, selective to the pad oxide. Subsequently, 3 nm TiN layer was deposited by chemical vapor deposition (CVD), followed by tungsten deposition targeting a thickness of 20 nm. Two different methods were employed for the metal, physical vapor deposition (PVD) sputtering by DC power and atomic layer deposition (ALD).

ALE modification on patterned and blanket wafers was carried out in a Lam Research system Kiyo® with previously reported conditions.

The oxide removal step was conducted on a SCREEN SU-3X00 tool at atmospheric pressure and room temperature with 1 M HCl for 5 min and rotation rate of 10 revolution per minute (rpm). For the removal time a fresh solution is continuously dispensed on top of the wafer.

CRediT authorship contribution statement

Cinzia Chan: Writing – original draft, Visualization, Validation, Methodology, Investigation, Formal analysis, Data curation, Conceptualization. **Jean-François de Marneffe:** Investigation. **Christopher Gort:** Writing – review & editing, Investigation. **Jill Serron:** Writing – review & editing, Investigation. **Marta Agati:** Investigation. **Felix Seidel:** Investigation. **Jan P. Hofmann:** Writing – review & editing, Resources. **Stefan De Gendt:** Writing – review & editing, Supervision, Project administration, Methodology, Conceptualization. **Dennis H. van Dorp:** Writing – review & editing, Supervision, Resources, Project administration, Methodology, Funding acquisition, Conceptualization.

Declaration of competing interest

The authors declare that they have no known competing financial interests or personal relationships that could have appeared to influence the work reported in this paper.

Acknowledgements

We thank Sofie Vandenbroucke and Christophe Detaverniner from UGent, Belgium for their assistance in XRR measurements. We thank Farid Sebaai for his support in setting up the wet etching recipe on imec's pilot line 300 mm tool. This research has been supported by the MADEin4 project for Metrology Advances for Digitized ECS industry 4.0 under the Grant Agreement 826589 from the EU Framework Program for Research and Innovation HORIZON 2020. We thank Thermo Fisher Scientific in Bremen (Germany) for their help to enable ICP-MS/MS measurements, and MKS Instruments Deutschland (Germany) for providing the ozone generator used in this study. We are grateful to Efrain Altamirano Sanchez for management support and Gouri Sankar Kar for program coordination (IMEC, Belgium).

Appendix A. Supplementary data

Supplementary data to this article can be found online at https://doi.org/10.1016/j.apsusc.2025.164983.

Data availability

Data will be made available on request.

References

[1] D. Choi, K. Barmak, On the potential of tungsten as next-generation semiconductor interconnects, Electron. Mater. Lett. 13 (2017) 449–456, https://doi.org/10.1007/s13391-017-1610-5.
[2] G. Thareja, A. Pal, Q. Ma, C. Ching, S. Patel, X. Gao, S. Dag, Z. Qi, A. Zhang, S. Yue, W. Lei, Y. Xu, Y. Lei, H. Jiang, S. You, W. Zheng, R. Hung, G. Costrini, Q. Zhu, R. Tran, R. Gupta, V. Reddy, P.B. Vyas, S. Hassan, M.P. Cai, G. Shen, Z. Chen, W. Hou, J. Lei, R. Wang, W. Shen, S. Deshpande, S. Huey, J. Tang, M. Naik, S. Kesapragada, B. Ayyagari-Sangamali, E.M. Bazizi, X. Tang, Tungsten interconnect resistance reduction enabling energy efficient and high performance applications for 2nm node and beyond, Int. Electron Devices Meet. (2023) 1–4, https://doi.org/10.1109/IEDM45741.2023.10413881.
[3] K. Ganesh, V.H. Gaidhane, Tungsten as an Interconnect Material for NextGeneration IC Design, in: 2020 IEEE Int. IOT, Electron. Mechatronics Conf., 2020, pp. 1–6, https://doi.org/10.1109/IEMTRONICS51293.2020.9216452.
[4] M. Rosmeulen, J. van Houdt, How can 3D FeFETs substitute NAND flash for low-latency storage, Electr. Des. News (2022). https://www.edn.com/how-can-3d-fefets-substitute-nand-flash-for-low-latency-storage/.
[5] J. Bakke, Extending tungsten metallization for next-generation devices, Solid State Technol. (2016) 26–29. https://sst.semiconductor-digest.com/2016/08/extending-tungsten-metallization-for-next-generation-devices/.
[6] J. Chatterjee, R.C. Sousa, N. Perrissin, S. Auffret, C. Ducruet, B. Dieny, Enhanced annealing stability and perpendicular magnetic anisotropy in perpendicular magnetic tunnel junctions using W layer, Appl. Phys. Lett. 110 (2017), https://doi.org/10.1063/1.4983159.
[7] M. Costa, A.T. Costa, J. Hu, R.Q. Wu, R.B. Muniz, β -tungsten : a promising metal for spintronics, J. Phys. Condens. Matter 30 (2018) 305802, https://doi.org/10.1088/1361-648X/aacc08.
[8] K. Kumar, V. Sethu, S. Ghosh, S. Couet, J. Swerts, B. Sorée, J. De Boeck, G.S. Kar, K. Garello, Optimization of tungsten β -phase window for spin-orbit-torque magnetic random-access memory, Phys. Rev. Appl 10 (2021) 1, https://doi.org/10.1103/PhysRevApplied.16.064009.
[9] F. Fang, Atomic and close-to-atomic scale manufacturing: perspectives and measures, Int. J. Extrem. Manuf. 2 (2020), https://doi.org/10.1088/2631-7990/aba495.
[10] G.S. Oehrlein, S.M. Brandstadter, R.L. Bruce, J.P. Chang, J.C. DeMott, V. M. Donnelly, R. Dussart, A. Fischer, R.A. Gottscho, S. Hamaguchi, M. Honda, M. Hori, K. Ishikawa, S.G. Jaloviar, K.J. Kanarik, K. Karahashi, A. Ko, H. Kothari, N. Kuboi, M.J. Kushner, T. Lill, P. Luan, A. Mesbah, E. Miller, S. Nath, Y. Ohya, M. Omura, C. Park, J. Poulose, S. Rauf, M. Sekine, T.G. Smith, N. Stafford, T. Standaert, P.L.G. Ventzek, Future of plasma etching for microelectronics: challenges and opportunities, J. Vac. Sci. Technol. B 42 (2024), https://doi.org/10.1116/6.0003579.

[11] C.T. Carver, J.J. Plombon, P.E. Romero, S. Suri, T.A. Tronic, R.B. Turkot, Atomic layer etching: an industry perspective, ECS J. Solid State Sci. Technol. 4 (2015) N5005–N5009, https://doi.org/10.1149/2.0021506jss.

[12] G.S. Oehrlein, D. Metzler, C. Li, Atomic layer etching at the tipping point: an overview, ECS Solid State Sci. Technol. 4 (2015) N5041–N5053, https://doi.org/10.1149/2.0061506jss.

[13] K.J. Kanarik, T. Lill, E.A. Hudson, S. Sriraman, S. Tan, J. Marks, V. Vahedi, R. A. Gottscho, Overview of atomic layer etching in the semiconductor industry, J. Vac. Sci. Technol. A Vacuum, Surfaces, Film. 33 (2015) 020802, https://doi.org/10.1116/1.4913379.

[14] C. Fang, Y. Cao, D. Wu, A. Li, Thermal atomic layer etching: Mechanism, materials and prospects, Prog. Nat. Sci.: Mater. Int. 28 (2018) 667–675, https://doi.org/10.1016/j.pnsc.2018.11.003.

[15] A. Fischer, A. Routzahn, S.M. George, T. Lill, Thermal atomic layer etching: a review, J. Vac. Sci. Technol. A Vacuum, Surfaces, Film. 39 (2021) 030801, https://doi.org/10.1116/6.0000894.

[16] K.J. Kanarik, S. Tan, R.A. Gottscho, Atomic layer etching: rethinking the art of etch, J. Phys. Chem. Lett. 9 (2018) 4814–4821, https://doi.org/10.1021/acs.jpclett.8b00997.

[17] S.M. George, Mechanisms of thermal atomic layer etching, Acc. Chem. Res. 53 (2020) 1151–1160, https://doi.org/10.1021/acs.accounts.0c00084.

[18] T. Faraz, H. Knoops, B. Macco, A. Mackus, V. Vandalon, E. Kessel, Atomic Limits ALE database, (access year 2025). https://doi.org/10.6100/aledatabase.

[19] K. Eriguchi, Modeling of defect generation during plasma etching and its impact on electronic device performance - plasma-induced damage, J. Phys. D Appl. Phys. 50 (2017), https://doi.org/10.1088/1361-6463/aa7523.

[20] C. Chan, D.H. van Dorp, S. De Gendt, J.-F. de Marneffe, Halogen impact on MTJ magnetic properties (Manuscript in preparation), (2025).

[21] N.D. Altieri, J.-K.-C. Chen, J.P. Chang, Controlling surface chemical states for selective patterning of CoFeB, J. Vac. Sci. Technol. A 37 (2019) 011303, https://doi.org/10.1116/1.5063662.

[22] W. Xie, G.N. Parsons, Thermal atomic layer etching of metallic tungsten via oxidation and etch reaction mechanism using O_2 or O_3 for oxidation and WCl_6 as the chlorinating etchant, J. Vac. Sci. Technol. A Vacuum, Surfaces, Film. 38 (2020) 022605, https://doi.org/10.1116/1.5134430.

[23] W. Xie, P.C. Lemaire, G.N. Parsons, Thermally driven self-limiting atomic layer etching of metallic tungsten using WF_6 and O_2, ACS Appl. Mater. Interfaces 10 (2018) 9147–9154, https://doi.org/10.1021/acsami.7b19024.

[24] N.R. Johnson, S.M. George, Wo,, 3 and W thermal atomic layer etching using "conversion-fluorination" and "oxidation-conversion-fluorination", Mechanisms (2017) https://doi.org/10.1021/acsami.7b09161.

[25] K. Shinoda, N. Miyoshi, H. Kobayashi, Y. Hanaoka, M. Izawa, K. Ishikawa, M. Hori, Plasma-assisted thermal-cyclic atomic-layer etching of tungsten and control of its selectivity to titanium nitride, J. Vacuum Sci. Technol. B. (2022), https://doi.org/10.1116/6.0001660.

[26] D.S. Kim, J.E. Kim, W.O. Lee, J.W. Park, Y.J. Gill, B.H. Jeong, G.Y. Yeom, Anisotropic atomic layer etching of W using fluorine radicals/oxygen ion beam, Plasma Process. Polym. 16 (2019), https://doi.org/10.1002/ppap.201900081.

[27] K. Saidov, I. Erofeev, Z. Aabdin, A. Pacco, H. Philipsen, A.W. Hartanto, Y. Chen, H. Yan, W.W. Tjiu, F. Holsteyns, U. Mirsaidov, Controlled stepwise wet etching of polycrystalline Mo nanowires, Adv. Funct. Mater. 34 (2024) 1–9, https://doi.org/10.1002/adfm.202310838.

[28] A. Pacco, Y. Akanishi, Q. Toan Le, Roughness and uniformity control during wet etching of molybdenum, Solid State Phenom. 314 (2021) 295–301, https://doi.org/10.4028/www.scientific.net/SSP.314.295.

[29] K. Sato, M. Shikida, T. Yamashiro, M. Tsunekawa, S. Ito, Roughening of single-crystal silicon surface etched by KOH water solution, Sensors Actuators A Phys. 73 (1999) 122–130, https://doi.org/10.1016/S0924-4247(98)00270-2.

[30] A. Pacco, Y. Akanishi, Q.T. Le, E. Kesters, G. Murdoch, F. Holsteyns, Controlled cobalt recess for advanced interconnect metallization, Microelectron. Eng. 217 (2019) 111131, https://doi.org/10.1016/j.mee.2019.111131.

[31] Y. Gong, R. Akolkar, Electrochemical atomic layer etching of ruthenium, J. Electrochem. Soc. 167 (2020) 62510, https://doi.org/10.1149/1945-7111/ab864b.

[32] M.R. Aziziyan, H. Sharma, J.J. Dubowski, Photo-atomic layer etching of GaAs/AlGaAs nanoheterostructures, ACS Appl. Mater. Interfaces 11 (2019) 17968–17978, https://doi.org/10.1021/acsami.9b02079.

[33] D.H. van Dorp, S. Arnauts, F. Holsteyns, S. De Gendt, Wet-chemical approaches for atomic layer etching of semiconductors: surface chemistry, oxide removal and reoxidation of InAs (100), ECS J. Solid State Sci. Technol. 4 (2015) N5061–N5066, https://doi.org/10.1149/2.0081506jss.

[34] N. Waldron, S. Sioncke, J. Franco, L. Nyns, A. Vais, X. Zhou, H.C. Lin, G. Boccardi, J.W. Maes, Q. Xie, M. Givens, F. Tang, X. Jiang, E. Chiu, A. Opdebeeck, C. Merckling, F. Sebaai, D. Van Dorp, L. Teugels, A.S. Hernandez, K. De Meyer, K. Barla, N. Collaert, Y.V. Thean, Gate-all-around InGaAs nanowire FETS with peak transconductance of 2200μS/μm at 50nm Lg using a replacement Fin RMG flow, in: 2015 IEEE International Electron Devices Meeting (IEDM), 2015, pp. 3111–3114, https://doi.org/10.1109/IEDM.2015.7409805.

[35] X. Zhou, N. Waldron, G. Boccardi, F. Sebaai, C. Merckling, G. Eneman, S. Sioncke, L. Nyns, A. Opdebeeck, J.W. Maes, Q. Xie, M. Givens, F. Tang, X. Jiang, W. Guo, B. Kunert, L. Teugels, K. Devriendt, A.S. Hernandez, J. Franco, D. Van Dorp, K. Barla, N. Collaert, A.V.Y. Thean, Scalability of InGaAs gate-all-around FET integrated on 300mm Si platform: demonstration of channel width down to 7nm and Lg down to 36nm, in: 2016 IEEE Symposium on VLSI Technology, 2016, pp. 1–2, https://doi.org/10.1109/VLSIT.2016.7573420.

[36] M. Konh, C. He, X. Lin, X. Guo, V. Pallem, R.L. Opila, A.V. Teplyakov, Z. Wang, B. Yuan, Molecular mechanisms of atomic layer etching of cobalt with sequential exposure to molecular chlorine and diketones, J. Vac. Sci. Technol. A 37 (2019) 021004, https://doi.org/10.1116/1.5082187.

[37] M. Magni, D. Scaccabarozzi, E. Palomba, E. Zampetti, B. Saggin, Characterization of thermal gradient effects on a quartz crystal microbalance, Sensors 22 (2022), https://doi.org/10.3390/s22197256.

[38] R. Fernández, M. Calero, Y. Jiménez, A. Arnau, A real-time method for improving stability of monolithic quartz crystal microbalance operating under harsh environmental conditions, Sensors 21 (2021), https://doi.org/10.3390/s21124166.

[39] J. Rip, D. Cuypers, S. Arnauts, F. Holsteyns, D.H. van Dorp, S. De Gendt, Etching of III-V materials determined by ICP-MS with Sub-nanometer precision, ECS J. Solid State Sci. Technol. 3 (2014) N3064–N3068, https://doi.org/10.1149/2.012401jss.

[40] D.H. van Dorp, S. Arnauts, M. Laitinen, T. Sajavaara, J. Meersschaut, T. Conard, J. J. Kelly, Nanoscale etching of III-V semiconductors in acidic hydrogen peroxide solution: GaAs and InP, a striking contrast in surface chemistry, Appl. Surf. Sci. 465 (2019) 596–606, https://doi.org/10.1016/j.apsusc.2018.09.181.

[41] G.H.A. Abrenica, M. Lebedev, M. Fingerle, S. Arnauts, N. Bazzazian, W. Calvet, C. Porret, H. Bender, T. Mayer, S. de Gendt, D.H. van Dorp, Atomic-scale investigations on the wet etching kinetics of Ge versus SiGe in acidic H2O2 solutions: a post operando synchrotron XPS analysis, J. Mater. Chem. C. Mater. Opt. Electron. Devices 8 (2020) 10060–10070.

[42] G.H.A. Abrenica, M.V. Lebedev, M. Fingerle, S. Arnauts, W. Calvet, T. Mayer, S. de Gendt, D.H. van Dorp, A synchrotron radiation photoelectron spectroscopy study on atomic-scale wet etching of InAs (111)-A and (111)-B in acidic peroxide solutions: surface chemistry versus kinetics, Mater. Today Chem. 23 (2022), https://doi.org/10.1016/j.mtchem.2021.100728.

[43] M.J.N. Pourbaix, Atlas of Electrochemical Equilibria in Aqueous Solutions, 1974. https://api.semanticscholar.org/CorpusID:93126068.

[44] M. Sharkass, S. Dwivedi, Y.K. Shin, M. Nieto-Perez, A.C.T. van Duin, P.S. Krstic, Oxidation of tungsten at room temperature irradiated by oxygen plasma, J. Phys. Chem. C (2024), https://doi.org/10.1021/acs.jpcc.4c03664.

[45] A. Romanyuk, V. Melnik, P. Oelhafen, Oxidation of tungsten surface with reactive oxygen plasma, Nucl. Instruments Methods Phys. Res. Sect. B Beam Interact. Mater. Atoms 232 (2005) 358–361, https://doi.org/10.1016/j.nimb.2005.03.073.

[46] E.A. Gulbransen, The kinetics of oxide film formation on metals and alloys, Trans. Electrochem. Soc. 91 (1947) 573, https://doi.org/10.1149/1.3071793.

[47] S. Takayanagi, Effect of oxygen pressure on the oxidation of tungsten powder, Trans. Japan Inst. Met. 3 (1962) 100–104, https://doi.org/10.2320/matertrans1960.3.100.

[48] S. Xu, L. Diao, Study of tungsten oxidation in $O_2/H_2/N_2$ downstream plasma, J. Vac. Sci. Technol. A Vacuum, Surfaces, Film. 26 (2008) 360–364, https://doi.org/10.1116/1.2897316.

[49] M. Claes, S. De Gendt, T. Witters, V. Kaushik, T. Conard, C. Zhao, Y. Manabe, A. Delabie, E. Rohr, J. Chen, W. Tsai, M.M. Heynsa, Effect of postdeposition anneal conditions on defect density of HfO[sub 2] layers measured by wet etching, J. Electrochem. Soc. 151 (2004) F269, https://doi.org/10.1149/1.1802134.

[50] H.F. Okorn-Schimdt, Characterization of silicon surface preparation processes for advanced gate dielectrics, IBM J. Researh Dev. 43 (1999) 351–365, https://doi.org/10.1016/j.jaci.2012.05.050.

[51] M.A. Pérez, M. López Teijelo, Ellipsometric study of dissolution of anodic WO_3 Films in aqueous solutions. 2. Reaction mechanism, J. Phys. Chem. B 109 (2005) 19369–19376, https://doi.org/10.1021/jp051102k.

[52] J.W. Johnson, E. Deng, S.C. Lai, W.J. James, The anodic dissolution of tungsten, J. Electrochem. Soc. 114 (1967) 424, https://doi.org/10.1149/1.2426620.

[53] M. Anik, K. Osseo-asare, Effect of pH on the anodic behavior of tungsten effect, Electrochem. Soc. (2002) B224–B233, https://doi.org/10.1149/1.1471544.

[54] M. Anik, T. Cansizoglu, Dissolution kinetics of WO3 in acidic solutions, J. Appl. Electrochem. 36 (2006) 603–608, https://doi.org/10.1007/s10800-006-9113-3.

[55] O. Kubaschewski, B.E. Hopkins, Oxidation mechanisms of niobium, tantalum, molybdenum and tungsten, J. Less Common Met. 2 (1960) 172–180, https://doi.org/10.1016/0022-5088(60)90012-6.

[56] DAIYS-FUN – FG Surface Science – TU Darmstadt, (n.d.). https://www.mawi.tu-darmstadt.de/of/forschung_of/of_ausstattung/of_daisy_fun/index.en.jsp.

[57] Y. Polyak, Z. Bastl, XPS and factor analysis study of initial stages of cerium oxide growth on polycrystalline tungsten, Surf. Interface Anal. 47 (2015) 663–671, https://doi.org/10.1002/sia.5762.

[58] A. Marin, C.P. Lungu, C. Porosnicu, Influence of gaseous environments on beryllium–tungsten and tungsten surfaces investigated by XPS, J. Vac. Sci. Technol. A Vacuum, Surfaces, Film. 35 (2017), https://doi.org/10.1116/1.4972513.

[59] P. Chen, M. Baldwin, P.R. Bandaru, Hierarchically structured, oxygen deficient, tungsten oxide morphologies for enhanced photoelectrochemical charge transfer and stability, J. Mater. Chem. A 5 (2017) 14898–14905, https://doi.org/10.1039/c7ta04118g.

[60] E. Ciftyürek, B. Šmíd, Z. Li, V. Matolín, K. Schierbaum, Spectroscopic understanding of SnO2 and WO3 metal oxide surfaces with advanced synchrotron based; XPS-UPS and near ambient pressure (NAP) XPS surface sensitive techniques for gas sensor applications under operational conditions, Sensors (Switzerland) 19 (2019), https://doi.org/10.3390/s19214737.

[61] J.V. Rojas, M. Toro-Gonzalez, M.C. Molina-Higgins, C.E. Castano, Facile radiolytic synthesis of ruthenium nanoparticles on graphene oxide and carbon nanotubes, Mater. Sci. Eng. B 205 (2016) 28–35, https://doi.org/10.1016/j.mseb.2015.12.005.

[62] M. Mazur, D. Wojcieszak, A. Wiatrowski, D. Kaczmarek, A. Lubańska, J. Domaradzki, P. Mazur, M. Kalisz, Analysis of amorphous tungsten oxide thin

films deposited by magnetron sputtering for application in transparent electronics, Appl. Surf. Sci. 570 (2021), https://doi.org/10.1016/j.apsusc.2021.151151.
[63] M.S. El-Basiouny, S.A. Hassan, M.M. Hefny, On the electrochemical behaviour of tungsten: the formation and dissolution of tungsten oxide in sulphuric acid solutions, Corros. Sci. 20 (1980) 909–917, https://doi.org/10.1016/0010-938X(80)90123-7.
[64] A. Di Paola, F. Di Quarto, G. Serravalle, A tensiostatic study of the anodic behaviour of tungsten in acid solutions, J. Less-Common Met. 42 (1975) 315–324, https://doi.org/10.1016/0022-5088(75)90051-X.
[65] S.E.S.E. Wakkad, H.A. Rizk, I.G. Ebaid, The electrochemical behavior of the tungsten electrode and the nature of the different oxides of the metal, J. Phys. Chem. 59 (1955) 1004–1008, https://doi.org/10.1021/j150532a003.
[66] A.A. Holder, Chromium, molybdenum and tungsten, Annu. Reports Prog. Chem. - Sect. A 109 (2013) 119–130, https://doi.org/10.1039/c3ic90005c.
[67] D. Wesolowski, H. Ohmoto, S.E. Drummond, R.E. Mesmer, Hydrolysis equilibria of tungsten(VI) in aqueous sodium chloride solutions to 300 °C, Inorg. Chem. 23 (1984) 1120–1132, https://doi.org/10.1021/ic00176a022.
[68] A.J. Bard, Standard potentials in aqueous solution, Dekker, New York (N.Y.), 1985.
[69] H. Philipsen, K. Vandersmissen, A. Cockburn, D. Erickson, C. Drijbooms, A. Moussa, H. Bender, H. Struyf, Metrology for Monitoring and Detecting Process Issues in a TSV Module, ECS J. Solid State Sci. Technol. 3 (2014) Q109–Q119, https://doi.org/10.1149/2.005406jss.
[70] A. Glavic, M. Björck, GenX 3: the latest generation of an established tool, J. Appl. Crystallogr. 55 (2022) 1063–1071, https://doi.org/10.1107/S1600576722006653.